Soft Matter

PAPER

View Article Online
View Journal | View Issue

Cite this: *Soft Matter*, 2017, **13**, 1654

Patterning of perovskite–polymer films by wrinkling instabilities†

G. Nasti,[abc] S. Sanchez,[d] I. Gunkel,[d] S. Balog,[d] B. Roose,[d] B. D. Wilts,[d] J. Teuscher,[e] G. Gentile,[b] P. Cerruti,[b] V. Ambrogi,[a] C. Carfagna,[b] U. Steiner[d] and A. Abate*[d]

Received 22nd November 2016,
Accepted 25th January 2017

DOI: 10.1039/c6sm02629j

rsc.li/soft-matter-journal

Organic–inorganic perovskites are semiconductors used for applications in optoelectronics and photovoltaics. Micron and submicron perovskite patterns have been explored in semitransparent photovoltaic and lasing applications. In this work, we show that a polymeric medium can be used to create a patterned perovskite, by using a novel and inexpensive approach.

1. Introduction

Organic–inorganic perovskites are crystalline materials with the general formula ABX_3, where A is an organic cation, B is a divalent metal cation and X is a halide anion. The metal cations coordinate 6 halide ions in an octahedral shape and the organic ions are located in cuboctahedral cavities coordinating 12 halide ions within the crystal lattice.[1] They have been employed as crystalline semiconductors with high optical density,[2] excitonic behavior[3] and long-range ambipolar charge transport.[4] Compared to traditional inorganic semiconductors, organic–inorganic perovskites are made of abundant, low-cost starting compounds. They are solution processable and thus compatible with fast and inexpensive production techniques. Since the first pioneering studies of Mitzi in the 90s,[5] organic–inorganic perovskites have been used in a number of optoelectronic applications such as photovoltaics,[6,7] photodetectors,[8] light emitting diodes,[9] transistors[10] and memory devices.[11] Their application in solar cells is most impressive, allowing the creation of solution processed devices with power conversion efficiencies that rival those of established inorganic technologies, only a few years after a first demonstration by Miyasaka *et al.* in 2009.[7,12,13] Furthermore, Eperon *et al.*[14] demonstrated the possibility of manufacturing semitransparent perovskite solar cells, which are particularly desired for building integration. Compared to other semi-transparent photovoltaic devices, they are highly color-neutral. Transparency is achieved by means of dewetting of the perovskite absorbing layer, resulting in the spontaneous formation of discrete micron-sized perovskite domains during the sample preparation process. In contrast, uniform perovskite deposition was enhanced by adding a small amount of poly(2-ethyl-2-oxazoline) (PEOXA) to the precursor solution.[15] More recently, patterning of perovskites on submicron length scales was explored for the preparation of optical cavities to enhance the light amplification in light-emitting and laser diodes.[16] Cheng *et al.* showed that luminescent patterned perovskite films can be obtained using soft lithography.[17] Sutherland *et al.* also demonstrated the possibility of achieving coherent light emission by deposition of a thin perovskite layer into a spherical optical cavity.[18] More recently, Alias *et al.*[19] reported a new patterning procedure based on a focused-ion beam technique to pattern perovskites on micron and submicron length scale for photonic devices. While these successful applications demonstrate the enormous potential of patterned perovskite films, most of these approaches involve several processing steps and, more importantly, are not easily scalable.

In this work, we introduce a novel approach for patterning perovskite crystals on a flat substrate. The novelty lies in the exploitation of a polymeric medium as the carrier of perovskite microcrystals. A long-range uniform patterning of the polymer was achieved by spontaneous wrinkling of the perovskite–polymer film in an oxygen plasma. The perovskite microcrystals were preferentially localized within the wrinkles of the film, transferring the polymer pattern to the perovskite assembly. Atomic force microscopy and dynamic light scattering showed that the dimensions of the wrinkles and the perovskite crystals can be tuned simply by controlling

[a] *Department of Chemical, Materials and Production Engineering, University of Naples "Federico II", Piazzale Tecchio 80, 80125 Napoli, Italy*
[b] *Institute for Polymers, Composites and Biomaterials (IPCB-CNR), via Campi Flegrei 34, 80078 Pozzuoli (NA), Italy*
[c] *Institute of Applied Sciences and Intelligent System, Via Campi Flegrei 34, Pozzuoli (NA), Italy*
[d] *Adolphe Merkle Institute, University of Fribourg, Chemin des Verdiers 4, CH-1700 Fribourg, Switzerland. E-mail: antonioabate83@gmail.com*
[e] *Group for Photochemical Dynamics, Institute of Chemical Sciences and Engineering, École Polytechnique Fédérale de Lausanne, Station 6, CH-1015 Lausanne, Switzerland*

† Electronic supplementary information (ESI) available. See DOI: 10.1039/c6sm02629j

the thickness of the polymer film and the perovskite precursor concentration.

2. Materials and methods

2.1. Materials

Fluorine doped tin oxide (FTO) coated glass slides and all other chemicals were purchased from Sigma-Aldrich, except for methyl ammonium bromide which was purchased from TCI Deutschland Gmbh. All chemicals were used as received.

2.2. PEGDA thin films wrinkling

Polyethylene glycol diacrylate (PEGDA) films were prepared using a Laurell WS-400BZ spin coater. PEGDA was crosslinked using a Zepto Diener (40 kHz, 100 W max power) plasma etcher. The chamber was first evacuated and then flushed with pure O_2 for 2 min to remove any residual N_2. PEGDA was then crosslinked by exposing the polymer films to an O_2 plasma for 30 s at a power of 50 W.

2.3. Perovskite crystals synthesis

$CH_3NH_3PbBr_3$ perovskite microcrystals were synthesized and functionalized with octylammonium iodide (OAI) alkyl chains. The perovskite crystals were prepared from a precursor solution of methylammonium bromide (MABr), octyl ammonium iodide (OAI) and lead bromide ($PbBr_2$) in *N*,*N*-dimethylformamide (DMF). Three different 1.0 M solutions of MABr, OAI and $PbBr_2$ in DMF were prepared. MABr and $PbBr_2$ solutions were mixed at a 1 : 1 volume ratio for non-OAI-capped crystals leading to a 0.5 M solution of (OAI)PbBr2. For capped crystals $PbBr_2$, MABr and OAI solutions were mixed at volume ratios of 10 : 9 : 1 resulting in a 0.5 M solution of $(MABr)_x(OAI)_{1-x}PbBr_2$ with x equal to 0.1. 0.1 M and the 0.01 M solutions of $(MABr)_x(OAI)_{1-x}PbBr_2$ were prepared by diluting a corresponding 0.5 M solution with measured amounts of DMF. Crystals were formed upon slow injection of one of the precursor solutions into 2 mL of toluene under intense stirring. Each injection consisted of 5 μL of precursor with a total volume injected of 50 μL. The total volume of precursor solution was kept constant for the three cases (0.5 M, 0.1 M and 0.01 M) to reduce the potential dissolution and recrystallization of dispersed crystals by residual DMF. The final volume ratio between DMF and toluene was 2.5% v/v. To remove any residual DMF and thus prevent undesired dissolution of the crystals during spin-coating as well as subsequent evaporation of toluene, we adopted a centrifuge separation routine. The dispersion was centrifuged at 10 000 rpm for 5 min (Mikro 20 centrifuge, Hettich, Germany) resulting in a precipitation of the crystals. The supernatant toluene/DMF solution was slowly removed and then an equal volume amount of toluene was added. This procedure was performed twice.

2.4. Characterization techniques

The formation of wrinkles was checked using a Zeiss Axio Scope.A1 optical microscope in transmission mode.

Fluorescence microscopy was performed using an Olympus BX51 microscope equipped with an X-Cite (series 120Q) LED-light as UV source.

Scanning electron microscopy (SEM) images were obtained with a Tescan MIRA3 and a FEI Quanta 200 FEG scanning electron microscope, respectively.

JPK Instruments Nano Wizard II atomic force microscope (AFM) was used in intermittent contact mode (tapping) to characterize the topography of the wrinkle patterns.

X-ray diffraction (XRD) measurements were performed using a Powder XRD Philips PW1800. The 2θ parameter was varied between 10° and 90° with a step size of 0.02°.

Dynamic light scattering (DLS) measurements were carried out at 21 °C, with detection at 90°, using a 3D LS Spectrometer (LS Instruments AG, Switzerland).

UV-vis spectra were acquired using a Specord 210 Plus (Analytik Jena) spectrofluorimeter using 1 cm quartz cuvettes.

The thickness of PEGDA thin films was measured with an alpha-SE ellipsometer (J. A. Woollam Co., Inc., Lincoln, NE).

Photoluminescence measurements on perovskite filled films were performed using a Horiba Fluorolog FL 3-22 device.

3. Results and discussion

3.1. PEGDA Wrinkling

Wrinkling of thin films *via* an instability under compressive stresses leads to a micron and submicron patterning of polymers.[20,21] A facile way to obtain such a patterning is to fabricate films having two or more layers of different elastic moduli. The relaxation of a compressive stress, either uniaxially (*i.e.* by releasing an external load) or isotropically (*i.e.* through a contraction after thermal expansion or swelling), leads to spontaneous wrinkling of the stiffer layer to lower the total energy of the system. Evensen *et al.* demonstrated that it is possible to achieve controlled wrinkle patterns in argon plasma treated thin films of polydimethylsiloxane (PDMS). In their work, the Ar plasma fulfilled two functions, (1) it crosslinked the PDMS film and (2) it formed a thin silica surface layer with a higher elastic modulus than that of the remaining polymer.[22] Recently, Lee *et al.* pointed out that controlled wrinkling of a polystyrene (PS) thin film caused by consecutive plasma exposures created three-dimensional hierarchical patterns.[23] A similar result can be obtained by creating a crosslinking gradient across the thin polymer layer, as shown by Guvendiren *et al.*, who exploited the quenching of radicals from atmospheric O_2 during UV curing of a thin poly(hydroxyethyl methacrylate) (PHEMA) layer, employing ethylene glycol dimethacrylate, (EGDMA) as cross-linker and a photoinitiator.[24]

In the present work, the formation of wrinkles in thin polyethylene glycol diacrylate (PEGDA) films was induced by a crosslinking gradient that formed during an O_2 plasma treatment. Thin PEGDA films were prepared by spin coating PEGDA/toluene solutions, with polymer concentrations ranging from 5% to 25% (v/v), onto glass substrates with or without a conductive layer of FTO. The film thickness was controlled by adjusting both the concentration of PEGDA in toluene and the spin coating speed in the range of 2000 to 8000 rpm. The as-spun liquid PEGDA (M_n = 700 g mol^{-1}) films were immediately exposed to an O_2 plasma, which resulted in a change of the film appearance from transparent to whitish, caused by the

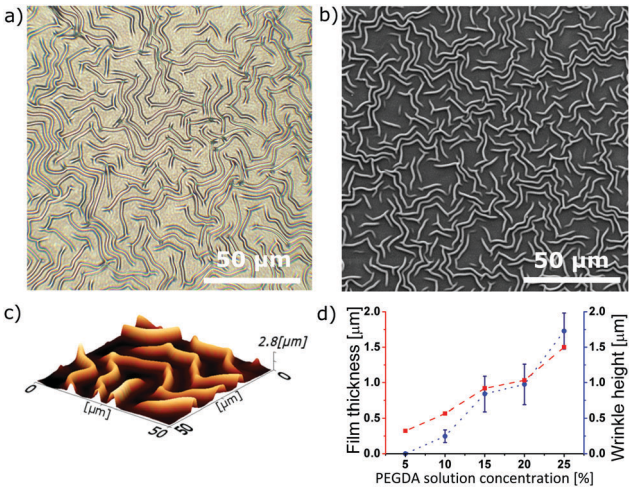

Fig. 1 Optical microscopy (a) and SEM (b) images of wrinkled PEGDA layers deposited on FTO-coated glass slides followed by an O_2 plasma treatment. (c) 3D AFM reconstruction of the wrinkle topography. (d) Variation of the PEGDA film thickness (before plasma curing, measured by ellipsometry) and wrinkle height (measured by AFM) with the solution concentration used to spin-coat the film, at a constant spinning speed.

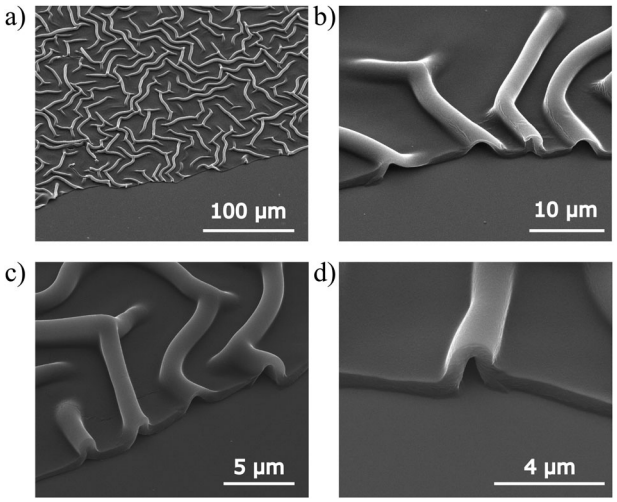

Fig. 2 SEM images of a section of a PEGDA wrinkled thin film (20 vol% PEGDA/toluene, spin coated at 6000 rpm) showing the thickness of the polymer layer and the morphology of the wrinkles.

increased light scattering from the wrinkles that have formed at the film surface. The formation of wrinkles was confirmed by optical microscopy in transmission, shown in Fig. 1a. The wrinkles were homogenously and isotropically distributed across the surface. The size and shape of the wrinkles were determined by SEM, shown in Fig. 1b. The half-cylindrical shape of the wrinkles gives rise to a focusing of light onto the cylinder axis. Note that the PEGDA film entirely covers the FTO substrate as confirmed by the absence of FTO crystals in the SEM image, which otherwise would be clearly visible (*cf.* Fig. 2a). The topography of the wrinkles was characterized by atomic force microscopy (AFM). Fig. 1c shows a 3D AFM image of a wrinkled PEGDA thin film that had an as-spun thickness of 1 μm before the O_2 plasma treatment. Both the width and height of the wrinkles are in the 1–3 μm range confirming their nearly cylindrical shape. As shown in Fig. 1d (*cf.* Fig. S1 and S2 in the ESI†) the wrinkle dimensions depend on the as-spun thickness of the PEGDA film and can be adjusted by varying the polymer solution concentration and the spinning speed during spin-coating. The buckled shape of the wrinkles is evident as can be seen in Fig. 2a–d (*cf.* Fig. S3, ESI†). The variation of the wrinkle dimensions (Fig. 1d, blue line) on the initial PEGDA film thickness (Fig. 1d, red line) agrees fairly with the Cerda and Mahadevan theory.[20]

3.2. Perovskite microcrystals

Obtaining well-dispersed perovskite microcrystals from PEGDA solutions requires the precise control of the processing conditions. Pérez-Prieto *et al.*[25,26] showed that highly luminescent and stable perovskite microcrystals can be prepared from a dispersion in toluene stabilized by alkyl ammonium chains at the crystal surface. It is well known that the material bandgap can be tuned by changing the halide composition[27] or the temperature of the precipitation solvent.[28] One of the first attempts to embed a perovskite phase in a dielectric polymeric matrix can be found in the work by Li *et al.*[29] who produced light emitting diodes (LEDs) with a remarkably improved external quantum efficiency. In a similar way Masi *et al.*[30] embedded perovskite microcrystals into a semiconducting polymer and manufactured a photovoltaic device with a power conversion efficiency (PCE) up to 3%.

Perovskite crystals were synthesized as described in Section 2.3. The color of the precursor solution turned from transparent to orange immediately after injecting its first drop into toluene, clearly indicating the formation of perovskite crystals. The need of the presence of OAI was evidenced by dispersion stability tests. Mixing MABr and $PbBr_2$ also led to the formation of an orange solution, but after a few minutes (less than 10 min) a precipitate was found on the bottom of the vial. After 24 h the solution became clear, indicating that all the perovskite crystals precipitated to the bottom. In contrast, crystals formed in the presence of OAI were very stable and only a small fraction of the crystals was found to precipitate after a week. The concentration of the precursor solution is another important control parameter of the formation of perovskite crystals. Three different precursor concentrations were tested: 0.5 M, 0.1 M and 0.01 M. The concentration of the precursor solution was found to affect both the crystal size and the dispersion stability, as demonstrated by DLS, which will be discussed in more detail in the following paragraph.

SEM images of the perovskite crystals deposited by drop casting the three solutions atop a FTO glass slide are shown in Fig. 3a (*cf.* Fig. S4, ESI†). The substrate was quickly heated to 150 °C to avoid recrystallization caused by residual DMF. The formed crystals were almost perfectly cubic with sizes below 500 nm but with relatively high polydispersity. DLS measurements of the perovskite dispersions were performed to study the effect of precursor concentration on the average size of the crystals. As shown in Fig. 3b a strong correlation between the

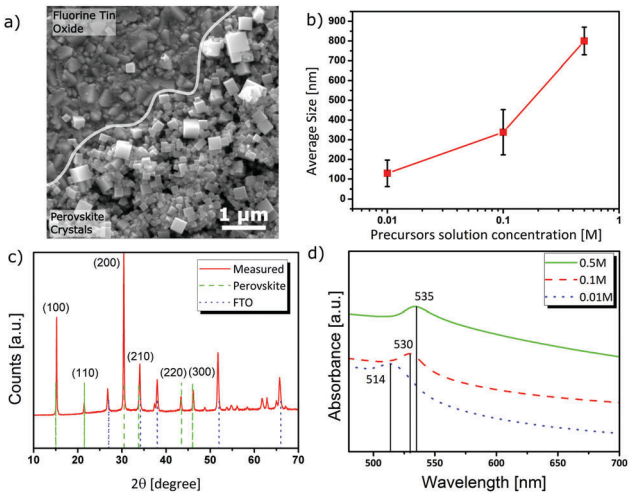

Fig. 3 (a) SEM image of perovskite crystals that have formed on top of a FTO covered glass slide. (b) DLS measurement showing a reduction of hydrodynamic crystal mean size with decreasing precursor solution concentration. (c) XRD measurement confirming the lattice structure of perovskite crystals. (d) UV-vis absorption spectra for crystals with different mean hydrodynamic radius; a blue shift of excitonic peak is clearly visible.

average hydrodynamic size and the molarity of the precursor solution was found, ranging from 800 nm for a 0.5 M solution to 130 nm for 0.01 M (average size distribution in Fig. S5, ESI†). The formation of $CH_3NH_3PbBr_3$ crystals was also investigated by X-ray diffraction (XRD). Fig. 3c shows narrow peaks that can be attributed to perovskite microcrystals and FTO crystals on the substrate.[26,31] The absorption spectra of Fig. 3d show that perovskite crystals obtained from the 0.5 M precursor solution were found to give rise to an excitonic peak at 535 nm and can be related to quantum confinement effects, as previously reported in literature.[3] This peak is clearly blue-shifted with decreasing average size of the crystals. While this effect has been observed previously by Di *et al.*, its origin is still debated.[32]

3.3. Composite

For the preparation of perovskite–polymer films, a toluene dispersion of perovskite crystals was mixed with PEGDA. It is important to emphasize that the OAI functionalization of perovskite crystals does not only stabilize the dispersion but also reduces the interaction between methylammonium cations and the acrylic groups of the polymer. When PEGDA was mixed with a toluene suspension of OAI-free perovskite crystals, the solution turned from orange to transparent within a few seconds. With OAI stabilized nanoparticles, no color change of the solution was observed. The mixed solutions of perovskite crystals and PEGDA in toluene were processed as described above for the case of pure PEGDA solutions to obtain wrinkle-patterned films. Optical micrographs of perovskite–polymer hybrid films after O_2 plasma treatment (Fig. 4a and Fig. S6, ESI†) confirm that perovskite crystals were preferably located inside the ridges of the PEGDA wrinkle pattern. This is further confirmed by fluorescence microscopy upon UV excitation, where the areas of the green emission of the perovskite crystals were found to coincide with the location of the wrinkles.

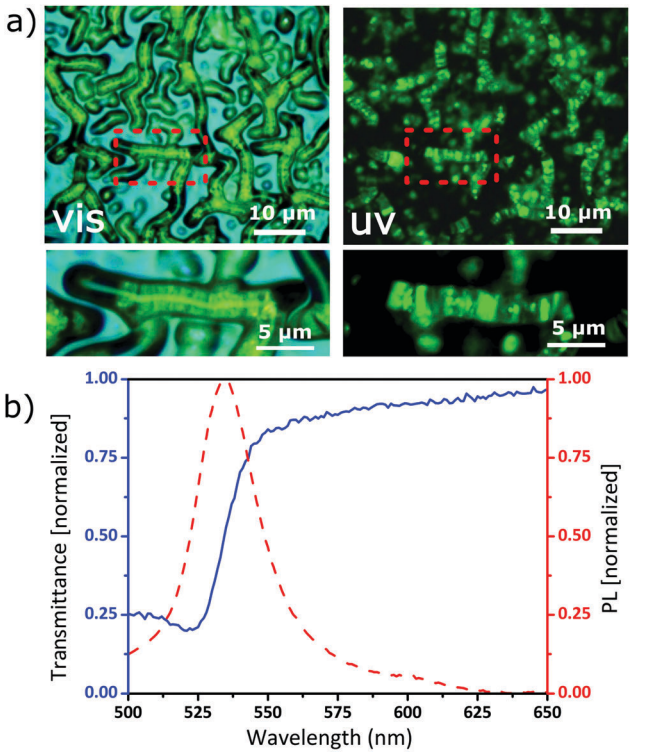

Fig. 4 Light microscopy images of wrinkle patterns filled with perovskite crystals. (a, top) White light illumination; (a, bottom) UV illumination. The perovskite microcrystals exhibit green fluorescence emission under UV light. Magnified images (a, right) evidence the efficient filling of wrinkles with nanoparticles. (b) Transmittance and emission spectra of perovskite crystals in the polymer. Green emission is clearly visible at 535 nm (dashed line) with the correspondent step-like absorbance transition (full line).

The localization of the perovskite crystals within the wrinkle morphology follows the mechanism that has been reported by Yoo *et al.*,[33] who demonstrated that most of the material composing the film moves to form wrinkles, and thus perovskite crystals dispersed within the film will be located within the wrinkles. In Fig. 4b (*cf.* Fig. S7, ESI†), transmittance and photoluminescence (PL) spectra of a wrinkled perovskite-containing film are shown. A step-like behavior in the transmittance and a sharp emission peak are clearly visible at 535 nm. However, it was not possible to quantify the emissive quantum efficiency due to the large size of the obtained crystals (~100 nm) which is too large to obtain a high enough dispersion of particles in solution and thus in the film.

4. Conclusions

We introduced a novel approach to patterning of perovskite–polymer films. Perovskite microcrystals dispersed in a polymer matrix were prepared by spin-coating a perovskite–polymer solution onto flat substrates. Micrometer patterning was induced by the spontaneous wrinkling of the perovskite–polymer film under an O_2 plasma. Perovskite microcrystals were predominantly located inside the ridge-structure formed by the polymeric wrinkles. This approach is potentially compatible with many different polymeric

matrices and patterning techniques and could therefore be exploited for optoelectronic applications. In contrast to the commonly used top-down patterning techniques, this approach enables solution processing and thus is potentially fast and inexpensive.

Acknowledgements

We acknowledge funding from the Swiss National Science Foundation under grant numbers 153990, 168223 and 141849. AA has received funding from the European Union's Seventh Framework Programme for research, technological development and demonstration under grant agreement no. 291771. GN acknowledges for financial support Campania Region (MASTRI Excellence Network – Materiali e strutture intelligenti – POR Campania 2007/2013). Helpful inputs from Michael Fischer and Manuel Kolly are gratefully acknowledged.

References

1 D. B. Mitzi, Templating and structural engineering in organic–inorganic perovskites, *J. Chem. Soc., Dalton Trans.*, 2001, 1–12.
2 S. D. Stranks, G. E. Eperon, G. Grancini, C. Menelaou, M. J. Alcocer, T. Leijtens, L. M. Herz, A. Petrozza and H. J. Snaith, Electron–Hole Diffusion Lengths Exceeding 1 Micrometer in an Organometal Trihalide Perovskite Absorber, *Science*, 2013, **342**(6156), 341–344.
3 V. D'Innocenzo, G. Grancini, M. J. Alcocer, A. R. S. Kandada, S. D. Stranks, M. M. Lee, G. Lanzani, H. J. Snaith and A. Petrozza, Excitons *versus* free charges in organo-lead tri-halide perovskites, *Nat. Commun.*, 2014, **5**, 3586.
4 Y. C. Hsiao, T. Wu, M. Li, Q. Liu, W. Qin and B. Hu, Fundamental physics behind high-efficiency organo-metal halide perovskite solar cells, *J. Mater. Chem. A*, 2015, **3**(30), 15372–15385.
5 D. Mitzi, C. Feild, W. Harrison and A. Guloy, Conducting tin halides with a layered organic-based perovskite structure, *Nature*, 1994, **369**(6480), 467–469.
6 N. J. Jeon, J. H. Noh, W. S. Yang, Y. C. Kim, S. Ryu, J. Seo and S. I. Seok, Compositional engineering of perovskite materials for high-performance solar cells, *Nature*, 2015, **517**(7535), 476–480.
7 A. Kojima, K. Teshima, Y. Shirai and T. Miyasaka, Organometal Halide Perovskites as Visible-Light Sensitizers for Photovoltaic Cells, *J. Am. Chem. Soc.*, 2009, **131**(17), 6050–6051.
8 L. Dou, Y. M. Yang, J. You, Z. Hong, W. H. Chang, G. Li and Y. Yang, Solution-processed hybrid perovskite photodetectors with high detectivity, *Nat. Commun.*, 2014, **5**, 5404.
9 Z. K. Tan, R. S. Moghaddam, M. L. Lai, P. Docampo, R. Higler, F. Deschler, M. Price, A. Sadhanala, L. M. Pazos, D. Credgington, F. Hanusch, T. Bein, H. J. Snaith and R. H. Friend, Bright light-emitting diodes based on organometal halide perovskite, *Nat. Nanotechnol.*, 2014, **9**(9), 687–692.
10 C. Kagan, D. Mitzi and C. Dimitrakopoulos, Organic-Inorganic Hybrid Materials as Semiconducting Channels in Thin-Film Field-Effect Transistors, *Science*, 1999, **286**(5441), 945–947.
11 Z. Xiao, Y. Yuan, Y. Shao, Q. Wang, Q. Dong, C. Bi, P. Sharma, A. Gruverman and J. Huang, Giant switchable photovoltaic effect in organometal trihalide perovskite devices, *Nat. Mater.*, 2015, **14**(2), 193–198.
12 W. S. Yang, J. H. Noh, N. J. Jeon, Y. C. Kim, S. Ryu, J. Seo and S. I. Seok, High-performance photovoltaic perovskite layers fabricated through intramolecular exchange, *Science*, 2015, **348**(6240), 1234–1237.
13 M. A. Green, K. Emery, Y. Hishikawa, W. Warta and E. D. Dunlop, Solar cell efficiency tables, *Prog. Photovoltaics*, 2015, **23**(1), 1–9.
14 G. E. Eperon, V. M. Burlakov, A. Goriely and S. J. Henry, Neutral color semitransparent microstructured perovskite solar cells, *ACS Nano*, 2014, **8**(1), 591–598.
15 Q. Xue, Z. Hu, C. Sun, Z. Chen, F. Huang, H. L. Yip and Y. Cao, Metallohalide perovskite–polymer composite film for hybrid planar heterojunction solar cells, *RSC Adv.*, 2015, **5**(1), 775–783.
16 G. Xing, N. Mathews, S. S. Lim, N. Yantara, X. Liu, D. Sabba, M. Grätzel, S. Mhaisalkar and T. C. Sum, Low-temperature solution-processed wavelength-tunable perovskites for lasing, *Nat. Mater.*, 2014, **13**(5), 476–480.
17 Z. Cheng, Z. Wang, R. Xing, Y. Han and J. Lin, Patterning and photoluminescent properties of perovskite-type organic/inorganic hybrid luminescent films by soft lithography, *Chem. Phys. Lett.*, 2003, **376**(3–4), 481–486.
18 B. R. Sutherland, S. Hoogland, M. M. Adachi, C. T. Wong and E. H. Sargent, Conformal Organohalide Perovskites Enable Lasing on Spherical Resonators, *ACS Nano*, 2014, **8**(10), 10947–10952.
19 M. S. Alias, I. Dursun, D. Shi, M. I. Saidaminov, E. M. Diallo, D. Priante, T. K. Ng, O. M. Bakr and B. S. Ooi, Focused-ion beam patterning of organolead trihalide perovskite for subwavelength grating nanophotonic applications, *J. Vac. Sci. Technol., B: Nanotechnol. Microelectron.: Mater., Process., Meas., Phenom.*, 2015, **33**(5), 051207.
20 E. Cerda and L. Mahadevan, Geometry and Physics of Wrinkling, *Phys. Rev. Lett.*, 2003, **90**(7), 074302.
21 J. E. Koskela, J. Vapaavuori, R. H. Ras and A. Priimagi, Light-Driven Surface Patterning of Supramolecular Polymers with Extremely Low Concentration of Photoactive Molecules, *ACS Macro Lett.*, 2014, **3**(11), 1196–1200.
22 H. T. Evensen, H. Jiang, K. Gotrik, F. Denes and R. Carpick, Transformations in Wrinkle Patterns: Cooperation between Nanoscale Cross-Linked Surface Layers and the Submicrometer Bulk in Wafer-Spun, Plasma-Treated Polydimethylsiloxane, *Nano Lett.*, 2009, **9**(8), 2884–2890.
23 W. K. Lee, C. J. Engel, M. D. Huntington, J. Hu and T. W. Odom, Controlled Three-Dimensional Hierarchical Structuring by Memory-Based, Sequential Wrinkling, *Nano Lett.*, 2015, 5624–5629.
24 M. Guvendiren, S. Yang and J. A. Burdick, Swelling-Induced Surface Patterns in Hydrogels with Gradient Crosslinking Density, *Adv. Funct. Mater.*, 2009, **19**(19), 3038–3045.
25 L. C. Schmidt, A. Pertegás, S. González-Carrero, O. Malinkiewicz, S. Agouram, G. Mínguez Espallargas, H. J. Bolink, R. E. Galian

and J. Pérez-Prieto, Nontemplate Synthesis of $CH_3NH_3PbBr_3$ Perovskite Nanoparticles, *J. Am. Chem. Soc.*, 2014, **136**(3), 850–853.

26 S. Gonzalez-Carrero, R. E. Galian and J. Perez-Prieto, Maximizing the emissive properties of $CH_3NH_3PbBr_3$ perovskite nanoparticles, *J. Mater. Chem. A*, 2015, **3**(17), 9187–9193.

27 F. Zhang, H. Zhong, C. Chen, X.-g. Wu, X. Hu, H. Huang, J. Han, B. Zou and Y. Dong, Brightly Luminescent and Color-Tunable Colloidal $CH_3NH_3PbX_3$ (X = Br, I, Cl) Quantum Dots: Potential Alternatives for Display Technology, *ACS Nano*, 2015, **9**(4), 4533–4542.

28 H. Huang, A. S. Susha, S. V. Kershaw, T. F. Hung and A. L. Rogach, Control of Emission Color of High Quantum Yield $CH_3NH_3PbBr_3$ Perovskite Quantum Dots by Precipitation Temperature, *Adv. Sci.*, 2015, **2**, 1500194.

29 G. Li, Z.-K. Tan, D. Di, M. L. Lai, L. Jiang, J. H. W. Lim, R. H. Friend and N. C. Greenham, Efficient Light-Emitting Diodes Based on Nanocrystalline Perovskite in a Dielectric Polymer Matrix, *Nano Lett.*, 2015, **15**(4), 2640–2644.

30 S. Masi, S. Colella, A. Listorti, V. Roiati, A. Liscio, V. Palermo, A. Rizzo and G. Gigli, Growing perovskite into polymers for easy-processable optoelectronic devices, *Sci. Rep.*, 2015, **5**, 7725.

31 S. H. Hsu, C. T. Li, H. T. Chien, R. R. Salunkhe, N. Suzuki, Y. Yamauchi, K. C. Ho and K. C. Wu, Platinum-Free Counter Electrode Comprised of Metal-Organic-Framework (MOF)-Derived Cobalt Sulfide Nanoparticles for Efficient Dye-Sensitized Solar Cells (DSSCs), *Sci. Rep.*, 2014, **4**, 6983.

32 D. Di, K. P. Musselman, G. Li, A. Sadhanala, Y. Ievskaya, Q. Song, Z. K. Tan, M. L. Lai, J. L. MacManus-Driscoll, N. C. Greenham and R. H. Friend, Size-Dependent Photon Emission from Organometal Halide Perovskite Nanocrystals Embedded in an Organic Matrix, *J. Phys. Lett.*, 2015, **6**(3), 446–450.

33 P. J. Yoo, K. Y. Suh, H. Kang and H. H. Lee, Polymer Elasticity-Driven Wrinkling and Coarsening in High Temperature Buckling of Metal-Capped Polymer Thin Films, *Phys. Rev. Lett.*, 2004, **93**(3), 034301.

Electronic Supplementary Material (ESI) for Soft Matter.

Supplementary Information

Patterning of perovskite-polymer films by wrinkling instabilities

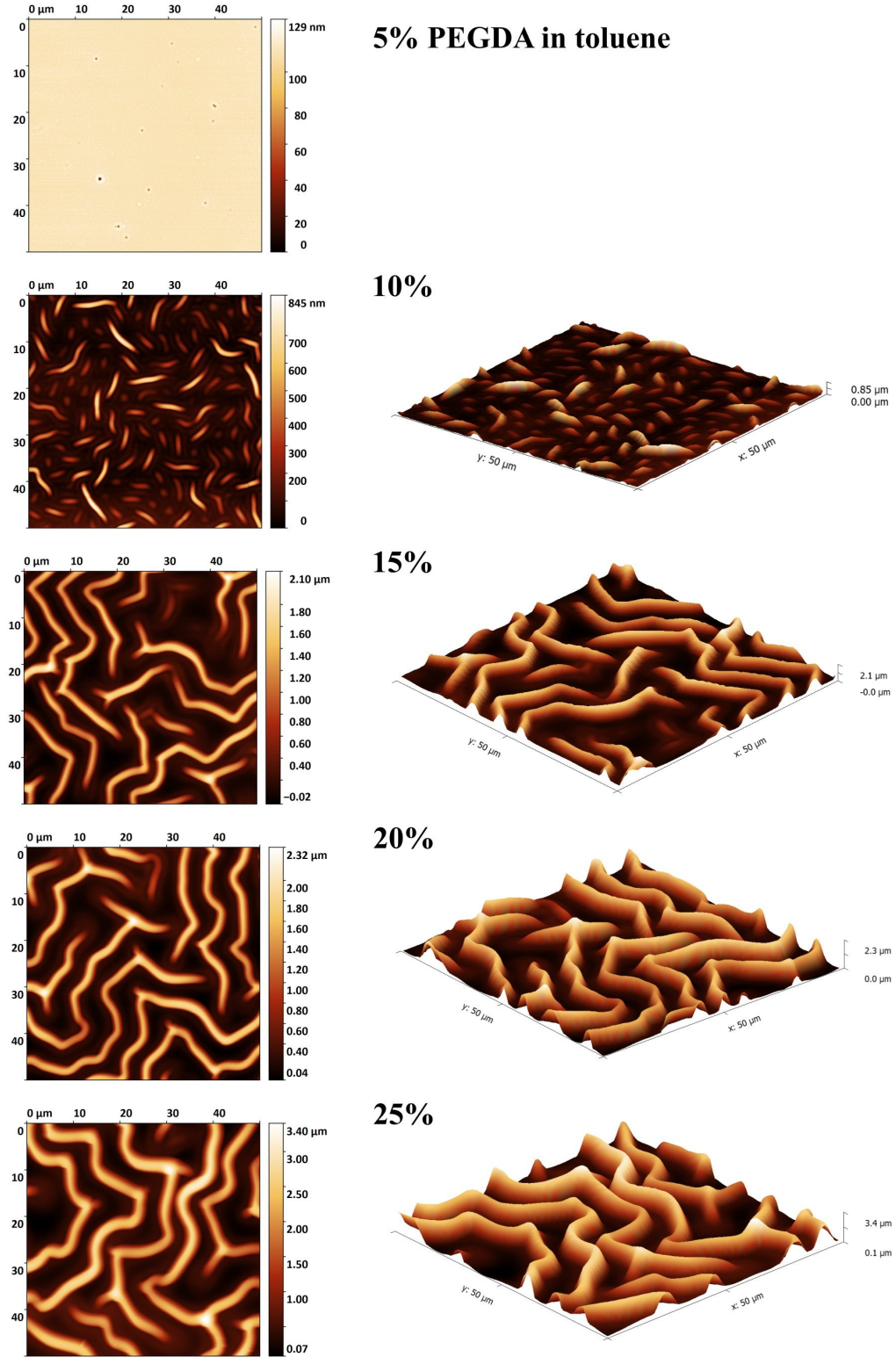

Figure S1 Atomic force microscopy (AFM) images of wrinkled PEGDA films after exposure to O_2 plasma. Films were prepared by spin-coating solutions of different PEGDA concentrations in toluene (5% to 25% (v/v)) atop FTO-coated glass at a constant spin-coating speed of 8000 rpm. The resulting films had a different initial thickness (c.f. Figure S2). It is evident that both the height and the width of the wrinkles increased with increasing PEGDA concentration (film thickness, c.f. Figure S2). While no wrinkles were observed for the lowest concentration (5%), the average height of the wrinkles was found to increase from 0.3 µm to 1.7 µm when increasing the polymer concentration from 10% to 25%.

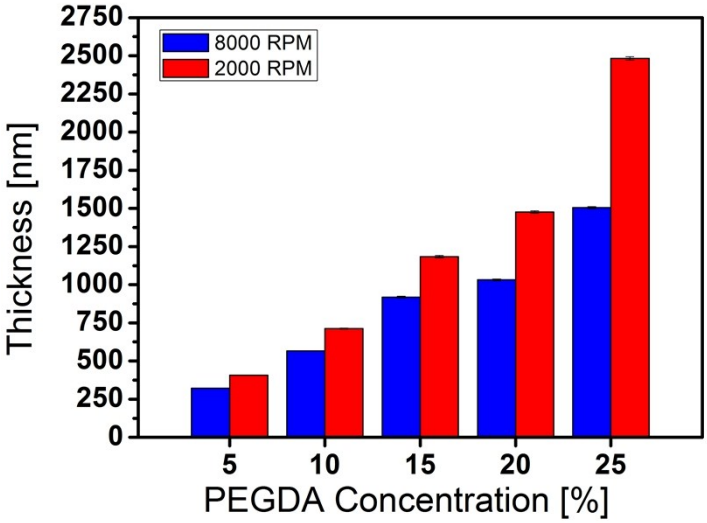

Figure S2 Thickness of PEGDA films as measured by means of ellipsometry as a function of the polymer concentration in toluene for two different spin-coating speeds. Changing both, the PEGDA concentration in toluene as well as spin-coating speed allowed for varying the thickness of PEGDA films between around 280 nm and about 2500 nm.

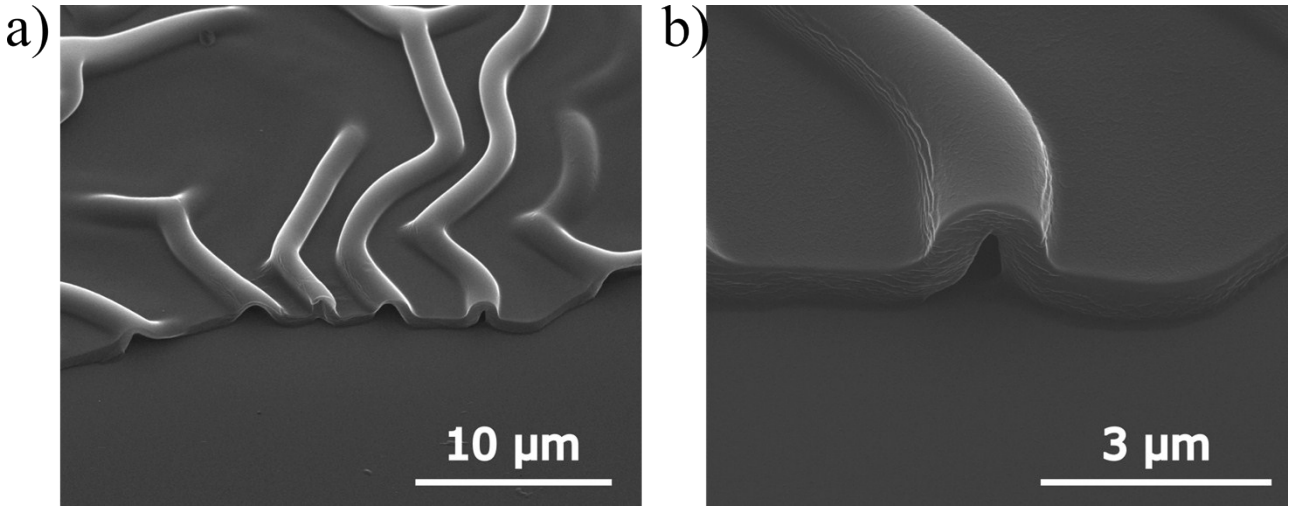

Figure S3 SEM image of a wrinkled PEGDA film (20 vol% PEGDA/toluene, spin coated at 6000 rpm) showing the thickness of the polymer layer and the shape of the wrinkles.

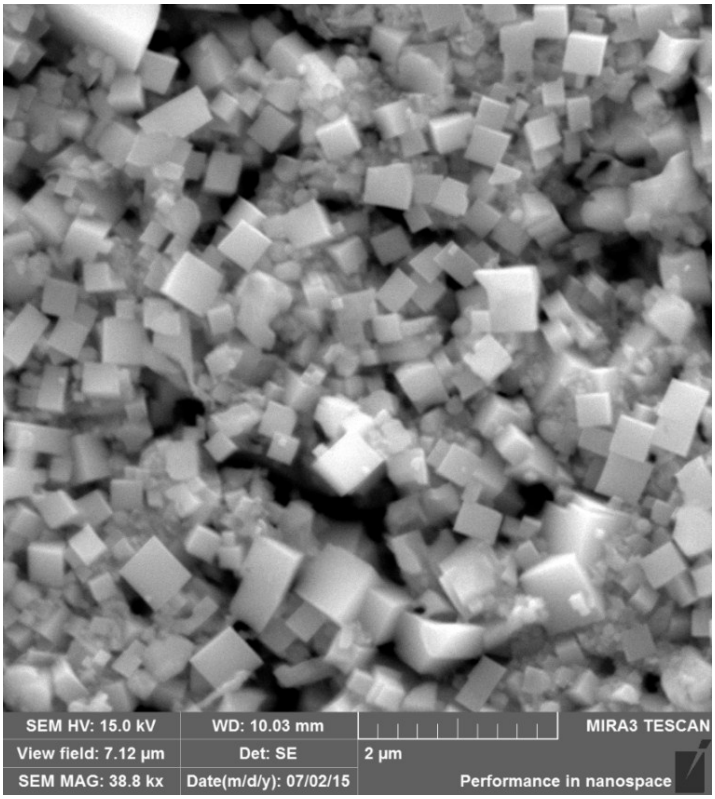

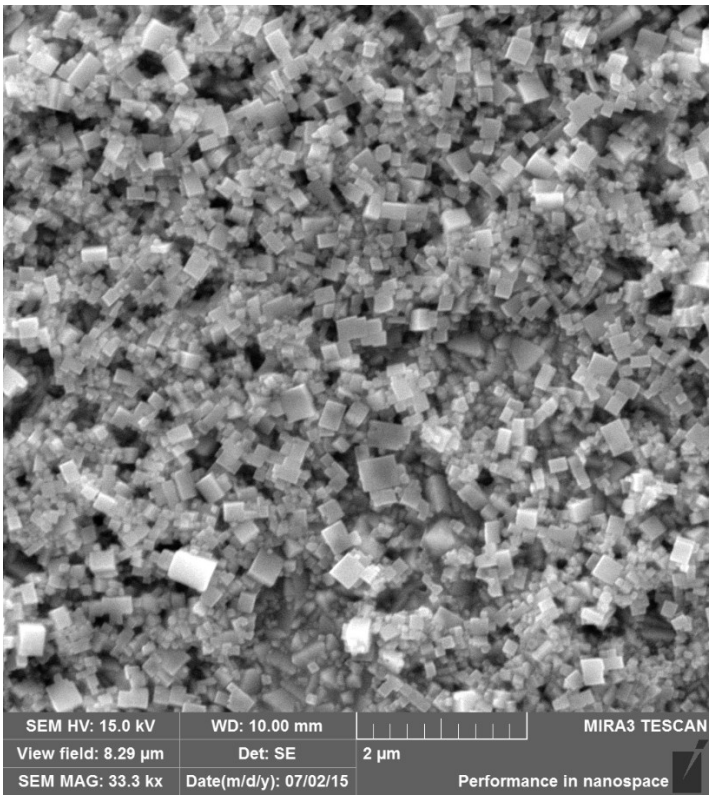

Figure S4 SEM images of perovskite nanocrystals synthesized from a 0.5 M (top) and 0.01 M (bottom) precursor solution.

Dynamic Light Scattering

Standard dynamic light scattering (DLS) data were collected at constant temperature (21 °C) at 90 deg., using a commercial goniometer instrument (3D LS Spectrometer, LS Instruments AG, Switzerland). The primary beam was formed by a linearly polarized and collimated laser beam (Cobolt 05-01 diode pumped solid state laser, λ = 660 nm, P_{max} = 500 mW), and the scattered light was collected by single-mode optical fibers equipped with integrated collimation optics. The collected light was coupled into two high-sensitivity APD detectors via laser-line filters (Perkin Elmer, Single Photon Counting Module), and their outputs were fed into a two-channel multiple-tau correlator. The signal-to-noise ratio was improved by cross-correlating these two channels. The corresponding field auto-correlation functions were obtained via the Siegert relation: $g_1(t) = \sqrt{g_2(t) - 1}$ where $g_2(t)$ is the intensity auto-correlation function constructed from the temporal fluctuations of the depolarized component of the scattered intensity.

For a dilute suspension of uniform spherical NPs of radius r, the correlation function is written as,

Equation 1
$$g_1(t) = e^{-\Gamma(q,r)t}$$

where

Equation 2
$$\Gamma(q,r) \equiv q^2 D_T$$

and

Equation 3
$$D_T = \frac{k_B T}{6 \pi \eta} \frac{1}{r}$$

k_B is the Boltzmann constant, T the temperature, η the viscosity of the solvent, q the momentum transfer $q = \frac{4\pi}{\lambda} n \sin\left(\frac{\theta}{2}\right)$, θ the scattering angle, λ the wavelength of the scattered waves, and n the refractive index of the solvent.

The field correlation function from polydisperse samples is frequently expressed as the Laplace transform of the probability density function describing the dispersion in the relaxation rate. Then the correlation function (Equation 1) is written as

$$g_1(t) = \int_0^\infty P(\Gamma)\, e^{-\Gamma t}\, d\Gamma$$

Equation 4

where $P(\Gamma)$ is the probability density function of the relaxation rates. $P_\Gamma(\Gamma)$ is modelled here by the (modified) Schulz–Zimm distribution:

$$P(\Gamma) = \frac{1}{\Gamma\left(\frac{1}{\sigma^2}\right)} e^{-\frac{\Gamma}{\langle\Gamma\rangle\,\sigma^2}} \left(\frac{1}{\langle\Gamma\rangle\,\sigma^2}\right)^{\frac{1}{\sigma^2}} \Gamma^{\frac{1}{\sigma^2}-1}$$

Equation 5

where

$$\langle\Gamma\rangle \equiv \int_0^\infty \Gamma P(\Gamma) d\Gamma$$

Equation 6

and

$$\sigma(\Gamma) \equiv \frac{\sqrt{var\Gamma}}{\langle\Gamma\rangle}$$

Equation 7

In case of a unimodal distribution $0 < \sigma \leq 1$. When σ is close to 1, the Schulz–Zimm distribution approaches an exponential distribution, and when σ is small, it approaches a Gaussian distribution. According to Equation 5, the correlation function is now written as

$$g_1(t) = \left(1 + \langle\Gamma\rangle\sigma^2 t\right)^{-\frac{1}{\sigma^2}}.$$

Equation 8

The correlation functions and their respective best fit (Figure S1, Equation 8) corresponding to the three different concentrations of the perovskite precursor solution are shown below. The estimated apparent intensity-weighted average hydrodynamic radii were 807 nm, 338 nm and 129 nm for 0.5M, 0.1M and 0.01M solutions, respectively. The intensity-weighted probability function of the hydrodynamic radius, $P_r(r)$, is estimated via applying the rule of transforming random variables. Let Φ represent the relationship between Γ and r (Equation 2 and 3). Then the probability density function of the intensity-weighted hydrodynamic radius is estimated via

$$P_r(r) = P_\Gamma(\Phi(r)) \cdot \left|\frac{d}{dr}\Phi(r)\right|$$

Equation 9

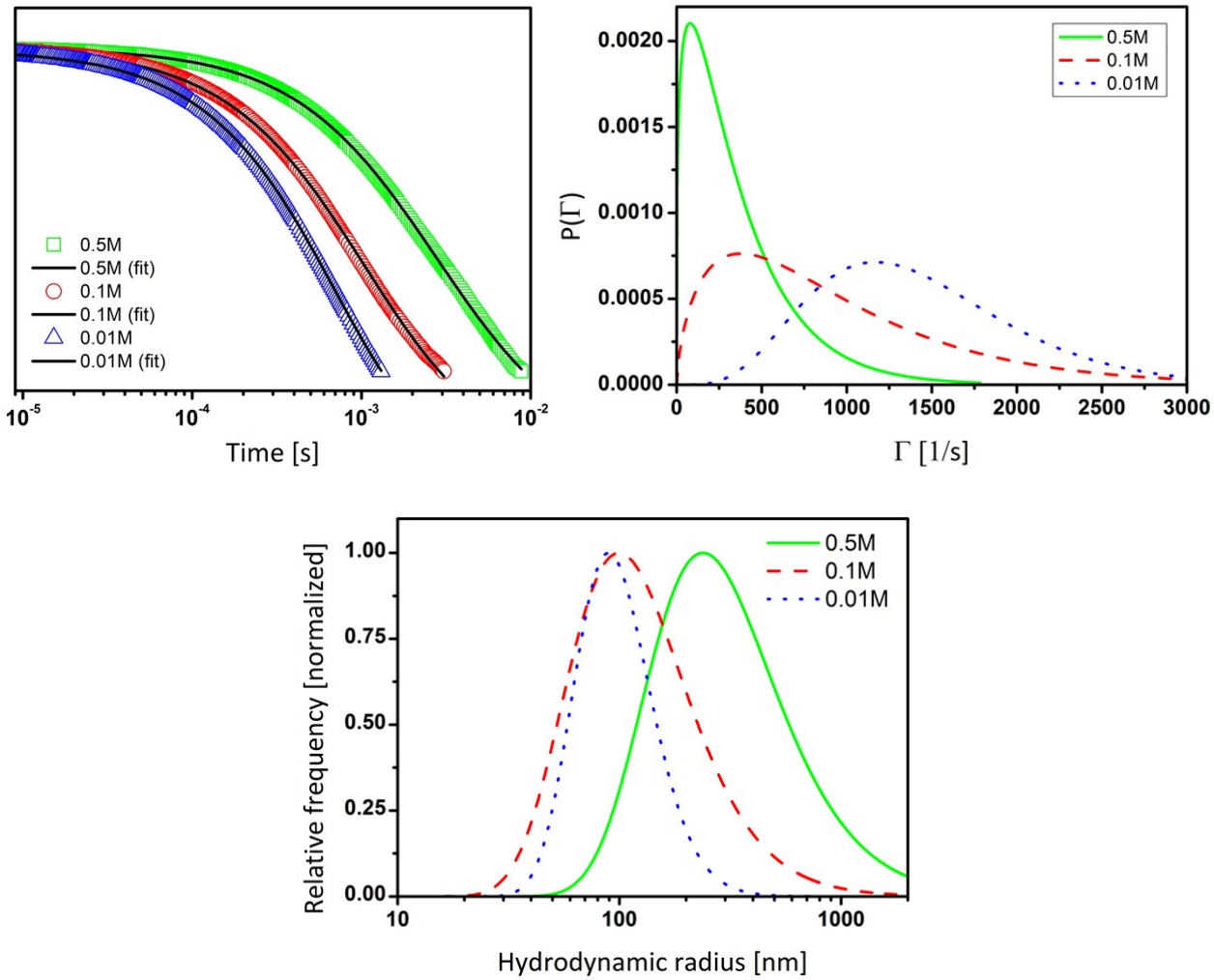

Figure S5 Correlation function and model fit (left) of the Equation 8 for 0.5M, 0.1M and 0.01M precursor solution concentrations (top left). Probability density function of the relaxation rates for the three samples (top right). Intensity-weighted probability density function of the hydrodynamic radius (bottom).

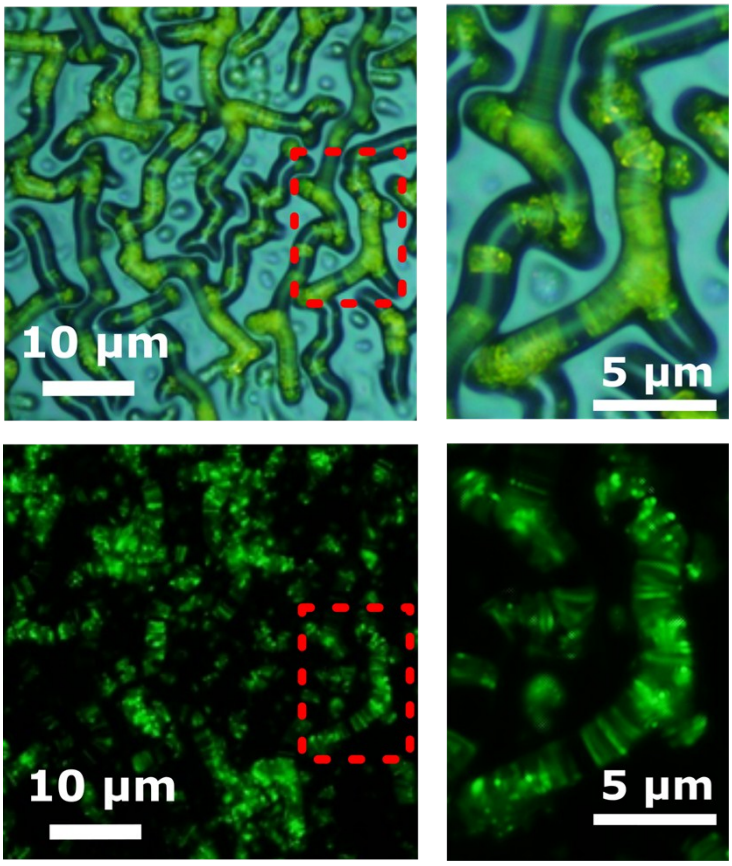

Figure S6 Preferential localization of perovskite crystals inside the ridges of a wrinkle pattern as shown by means of visible light microscopy (top) and under UV illumination (bottom). The green fluorescence emission of perovskite nanocrystals can be observed under UV light. Magnified images are shown on the right.

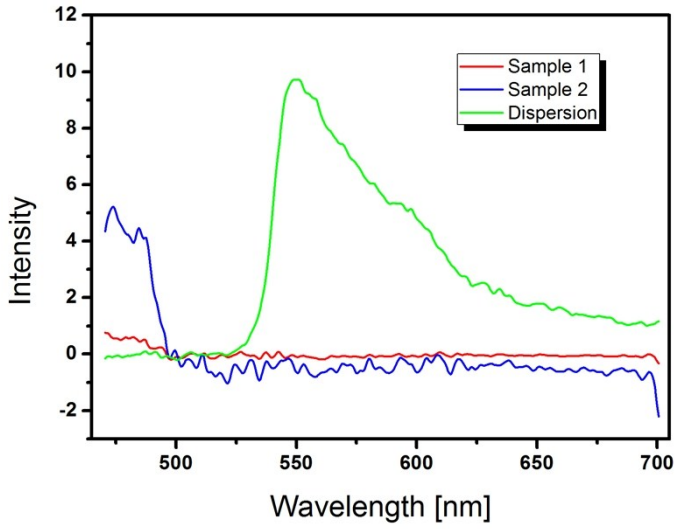

Figure S7 Photoluminescence spectra collected using an integrating sphere of a film with (Sample 1) and without the perovskite crystals (Sample 2) and toluene dispersion of perovskite crystals. The signal from the film is too weak to quantify the emissive efficiency. This is due to the fact that the smallest particle size obtained with the method in this work (100 nm) is too large to get a high enough dispersion of particles in solution and thus in the film.

Cerda and Mahadevan derived the following equations for the wavelength λ and amplitude *A* of wrinkles on a thin sheet of length *L*, width *W*, thickness *t*, elastic modulus *B*, imposed transverse displacement Δ, and tension *T*:

$$\lambda = 2\sqrt{\pi}\left(\frac{B}{T}\right)^{\frac{1}{4}} L^{\frac{1}{2}}$$

$$A = \frac{\sqrt{2}}{\pi}\left(\frac{\Delta}{W}\right)^{\frac{1}{2}} \lambda$$

For a stretched sheet these equation become:

$$\lambda = \frac{(2\pi L t)^{\frac{1}{2}}}{\left[3(1-\nu^2)\gamma\right]^{\frac{1}{4}}}$$

$$A = (\nu L t)^{\frac{1}{2}}\left[\frac{16\gamma}{3\pi^2(1-\nu^2)}\right]^{\frac{1}{4}}$$

So the amplitude of the wrinkles is dependent upon the thickness of the film with a power law dependence with exponent 0.5. So, using the basic properties of logarithms:

$$\log(A) \propto 0.5 \log(t) + C$$

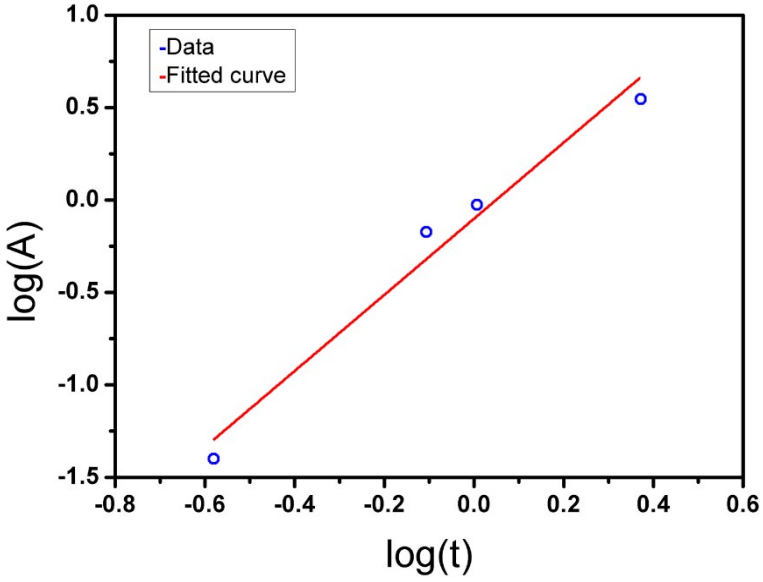

Figure S8. Linear best fit of the wrinkle amplitude as function of initial PEGDA film thickness (red line is a fit to: log(A)=a*log(t)+b; with a = 2.013; b = -0.1543).

Figure S7 reports the linear best fit of the logarithm of the wrinkle height as a function of the initial film thickness. Although the general behaviour is in agreement with the Cerda and Mahadevan theory (i.e. it is possible to increase the amplitude of the wrinkles by increasing the thickness of the film) the angular coefficient of the fitting line is ~2, far from the expected 0.5. This is probably due to the very simple model used, which approximates the PEGDA to a homogeneous film subjected to a compressive internal stress. In our case, the PEGDA film most probably has a longitudinal anisotropy with the elastic modulus varying throughout the thickness of the material, due to the different plasma exposure leading to a gradient in the crosslinking degree along the vertical direction (see Chandra et al, "Self-Wrinkling of UV-Cured Polymer Films", , *Advanced Materials*, 23(30), pp.3441-3445). We can approximate this system with a two-layer film

with a constant “hard skin” of thickness h_s and a varying “soft skin” of thickness h. So the total thickness will be $t=h_s+h$. In this approximation we can use the relationship found by Cerda and Mahadevan:

$$A \propto \lambda \propto (hh_s)^{\frac{1}{2}} \rightarrow \log(A) \propto 0.5 log(t - h_s)$$

because $h_s = h_s(t - h_s)$ and, using the properties of logarithms, $\log(h_s(t - h_s)) = \log(t - h_s) + const.$

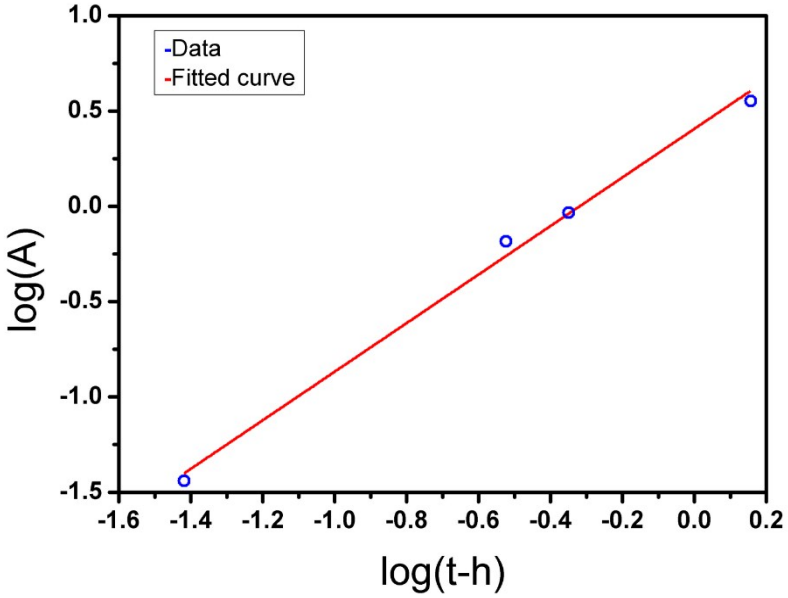

Figure S9. Linear best fit of wrinkles amplitude as function of initial PEGDA film thickness using the two-layer approximation (red line is fit to log(A)=a*log(t-h)+b; with h = 0.322; a = 1.246; b = 0.3921).

In Figure S9 the linear best fit of *log(A)* as function of *log(t-h_s)* is shown. The hard skin thickness has been chosen to be equal to 0.322 because for this thickness no wrinkles are formed (c.f. with Figs. 1d and S1). As we can see the angular coefficient of the fitting line is ~1.2, which is significantly closer to the angular coefficient of 0.5 predicted from the Cerda and Mahadevan model than the value we obtained with a simple homogeneous film approximation. This confirms our hypothesis that the anisotropy with the elastic modulus varying through the thickness makes our system more complex than a single or double layer film approximation of the Cerda and Mahadevan model.